



Fault spacing in continental strike-slip shear zones

Haibin Yang^{a,*}, Louis N. Moresi^{a,b}, Mark Quigley^a

^a School of Earth Sciences, University of Melbourne, Victoria, Australia

^b Research School of Earth Sciences, Australian National University, Canberra, Australia

ARTICLE INFO

Article history:

Received 1 May 2019

Received in revised form 2 October 2019

Accepted 10 October 2019

Available online 25 October 2019

Editor: A. Yin

Keywords:

San Andreas fault system

Marlborough Fault Zone

central Tibet

fault strength

lower crust viscosity

crust-mantle coupling

ABSTRACT

Strike-slip shear zones with sub-parallel arrays of evenly-spaced faults are widely observed in nature, but the controls on the spacing between major faults are unclear. We analyze a 2-D model and develop a scaling law relating the fault spacing to structural and rheological parameters in the continental crust. We find that fault spacing positively correlates with brittle-layer thickness, viscous lower crust thickness, and strength contrast between active faults and surrounding intact blocks; and is inversely correlative with lower crust viscosity. This is corroborated for either a zero-shear traction (decoupled) or a prescribed velocity (coupled) basal boundary condition in the 2-D analytical solution. The zero-shear traction boundary condition represents low viscosities in the lowermost crust or the topmost mantle that may decouple deformations from mantle flow. The prescribed velocity boundary condition emphasizes basal drag tractional forces imparted on the lower crust by a strong mantle. For a viscous layer that is thicker than half of its average fault spacing, models with either of the boundary conditions produce the same results. Otherwise, a thinner, viscous layer with a linear-velocity condition tends to produce smaller fault spacings than a no-shear model, all else being equal. These theoretical models are compared to data from shear zones in California, the Marlborough Fault Zone in New Zealand and central Tibet. Modeling indicates that the effective viscosity of the viscous layer underlying the brittle layer in all of the selected areas is 2×10^{20} to 4×10^{21} Pa-s. The subducted oceanic plate attached to the lower crust of the eastern Marlborough Fault Zone also appears to influence fault spacing in the overriding plate.

© 2019 Elsevier B.V. All rights reserved.

1. Introduction

Strike-slip faults are important features of plate tectonics on Earth (Wilson, 1965). Finite horizontal displacements on strike-slip faults at continental plate boundaries can reach several hundreds of kilometers, e.g., San Andreas fault (SAF, California) and Alpine fault (New Zealand). It is often assumed that such major strike-slip faults (i.e., continental transform faults) cut through entire lithosphere (Roy and Royden, 2000a). In contrast to a deep-penetrating transform fault, intraplate strike-slip (transcurrent) faults are often assumed to be limited to the thickness of crust and manifest as parallel arrays of nearly uniform spacing between neighboring faults, e.g., the East Californian Shear Zone (ECSZ) and the strike-slip fault systems surrounding Tibet (Yin and Taylor, 2011). Zusa et al. (2017) observed that active fault spacing in the ECSZ is tens of kilometers while in the Tibetan Plateau it is hundreds of kilo-

meters. Why fault spacing varies with different tectonic settings is not well understood.

The concept of stress-shadowing, which is widely used in explanations of extensional-joint spacing, was introduced by Yin et al. (2016) in the context of the mechanics of evenly-spaced faults. This mechanism was further developed by Zusa et al. (2017) to explain the spacing of faults in California and the India-Asia collision zone. Stress-shadow theory relates shear stress (σ_{xy}) to geometrical parameters (x , distance from the fault; h , depth of the fault) through a power law according to $\sigma_{xy}(x) = \sigma^{bc} + (\sigma^{bc} - \sigma^f) \left[\frac{|x|^{l_1/2}}{(|x|^{l_1} + h^{l_1})^{1/2}} - 1 \right]$ where σ^{bc} and σ^f are the far-field stress boundary condition and the vertically-averaged stress on the fault plane respectively. However, the exact values of the power-law exponent (l_1 and l_2) are unknown. Zusa et al. (2017) calibrated the exponent using sandbox modeling and suggested a linear relationship, i.e., both exponents, l_1 and l_2 , equal to one. It is not clear how sandbox results translate to other systems and how properties of the lower crust control brittle deformation patterns. Our analysis includes the effects of lower crustal flow to determine the expression of lower-crustal properties in surface strain distributions.

* Corresponding author.

E-mail address: haibiny@student.unimelb.edu.au (H. Yang).

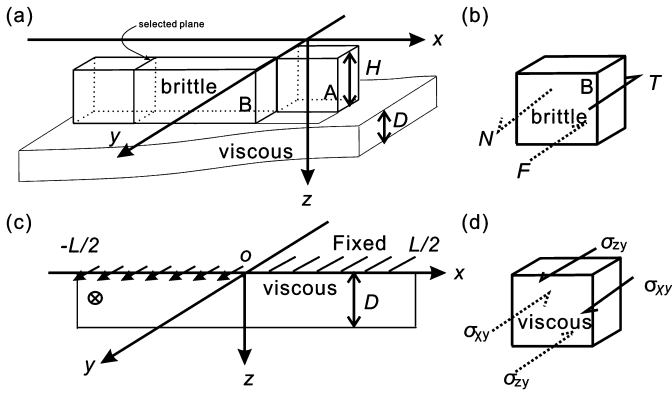


Fig. 1. (a) Schematic structure of a crustal strike-slip fault. Applied lateral forces break the brittle layer into two blocks, A and B, which are separated by a fault in-between. The fault cuts through the whole brittle layer thickness H . Select any vertical plane in B and do force balance analysis for the volume in B from the selected plane to the fault. It is balanced by the frictional force, T , from A, the viscous force, F , from the bottom and internal force, N , from the rest of B (b). (c) Sketch model for the lower layer of viscous rheology. The model length is L and thickness is D . The right half of the model is fixed, and the left half moves with a constant velocity V_0 . With the assumption of an infinite long strike-slip fault, only two nonzero stresses, σ_{xy} and σ_{zy} , work to balance the element (d).

Roy and Royden (2000a) presented an analytic model of the deformation of a stratified, viscoelastic crust driven by basal velocity boundary conditions. Their results showed that, a strong viscosity contrast between an upper and lower crust tends to produce a wide deformation zone. A relatively weak upper crust, if it reaches the yield stress, should have a more localized deformation zone than the case of a strong upper crust. From that perspective, in the limit of pure elastic deformation, we would expect faults to develop everywhere. Since the study assumes a fixed, shallow faulting-depth without considering pressure-dependence of the yield criterion, such a conclusion may only apply to surficial faults. We note that the model of Roy and Royden (2000a) is focused on plate boundary faults and the loading is applied from the underlying mantle. This choice may not be appropriate for intracrustal transcurrent faults overlying a weak lower crust. Rolandone and Jaupart (2002) proposed a model driven from far field stresses and suggested the fault depth and vertical variations in crustal rheology control deformation patterns. They found a deep fault or large vertical rheological variations help localize deformation on a pre-defined fault zone. However, scaling relationships for fault spacing were not explicitly examined in either of the studies.

In this contribution we first develop a scaling law for the emergent fault spacing in a stratified visco-plastic model. The model is composed of a brittle upper crust and a viscous lower crust. Faults are assumed to cut through the brittle upper layer and the brittle deformation terminates in the viscous layer (Fig. 1). The difficulty for the physical model lies in deriving a functional form of shear stress σ_{zy} at the bottom of a brittle layer. This basal shear stress σ_{zy} , in turn, influences the average shear stress σ_{xy} in the brittle crust (Savage and Lachenbruch, 2003). How shear stress, σ_{xy} , evolves from a fault towards the far field is the basis for the stress-shadow theory used by Zuza et al. (2017). Our analytical solutions demonstrate that the basal shear stress is a function of the aspect ratios of a model. We compare our scaling theory for fault spacing against field observations from the SAF system in California, the Marlborough Fault Zone (MFZ) in New Zealand and shear zones in the central Tibet. Modeling of fault spacing enables further refinement of viscosity parameters in the lower crust beneath those shear zones. Investigating structural parameters, e.g., seismogenic thickness, viscous layer thickness, and fault spacing, also

sheds light on the coupling state between shallower brittle deformation and deep dynamics.

2. Physical analysis

To determine controls on the spatial distribution of fault traces, we first assume a structurally and rheologically homogeneous material for our model. We acknowledge that re-activation of heterogeneous, pre-existing weak zones (e.g. inherited fault zones and lithologic contacts) are broadly observed in different tectonic settings (Quigley et al., 2010; Yang et al., 2018), and that these factors may influence fault spacing, however in this study we seek to develop a more fundamental understanding of lithospheric scale controls on fault spacing. We first make a force balance analysis for the upper brittle layer with a prescribed basal shear stress to obtain the first-order governing equation for fault spacing. Then, a more self-consistent model describing shear stress at the bottom of a brittle layer is derived as a solution to a Laplace equation.

2.1. Force balance analysis in brittle layer

Consider a system subject to simple shear from lateral boundaries (Fig. 1a). Applied boundary conditions produce localized frictional motion on discrete planes in the brittle upper layer and diffuse creep in the lower, viscous part. Suppose first that the applied stresses are high enough to break the upper layer into two pieces, block A and B (Fig. 1a). The right face of block B is sheared against block A, so the tangential force (T) on the fault plane can be derived from the integral of shear stress (σ_{xy}) in the z direction

$$T = \int_0^H \sigma_{xy} dz \quad (1)$$

where H is the cutting depth of a brittle fault, and

$$\sigma_{xy} = \mu_0 p \quad (2)$$

where μ_0 is the friction coefficient of a fault and p is the assumed normal stress on the vertical plane. Neglecting the effect of dynamic compressional or extensional forces, p can be simply taken as the lithostatic pressure

$$p = \rho g z \quad (3)$$

where ρ is the material density and g is the gravitational acceleration. With equations (2) and (3), equation (1) can be reformulated to

$$T = \int_0^H \mu_0 p dz = \int_0^H \mu_0 \rho g z dz = \frac{1}{2} \mu_0 \rho g H^2 \quad (4)$$

To calculate the viscous shear tractions on the base of block A, we assume a Newtonian fluid of a constant viscosity η in the lower layer, the basal shear stress, σ_{zy} , is given by the constitutive relation

$$\sigma_{zy} = 2\eta \dot{\epsilon}_{zy} \quad (5)$$

where $\dot{\epsilon}_{zy}$ is the corresponding strain rate. Long-term-average strain rates based on block models show that the second-invariant strain rate decays by more than 3 orders of magnitude within tens of kilometers of an active fault in the San Andreas fault system (Bird, 2009). We assume $\dot{\epsilon}_{zy}$ decays from $\dot{\epsilon}_0$ at the interface between A and B ($x = 0$) to zero at distance L , following a power law relationship. This yields

$$\dot{\varepsilon}_{zy}(x) = \dot{\varepsilon}_0 \left(1 - \frac{x}{L}\right)^m \quad (0 \leq x \leq L) \quad (6)$$

Integrating σ_{zy} in x gives the magnitude of the basal traction as

$$F(x) = \int_0^x \sigma_{zy} dx = 2\eta \dot{\varepsilon}_0 L \left[\frac{1}{m+1} - \frac{(1 - \frac{x}{L})^{m+1}}{m+1} \right] \quad (0 \leq x \leq L) \quad (7)$$

where x is the position of selected vertical plane parallel to y . The basal traction increases inwards from the fault and reaches a maximum at $x = L$. That is

$$F_{max} = \frac{2\eta \dot{\varepsilon}_0 L}{m+1} \quad (8)$$

The force balance requires the tangential force (N) in y on the selected vertical plane to be

$$N = T + F \quad (9)$$

where N , T and F are scalar magnitudes of the forces with orientations shown in Fig. 1b. In the case of faults driven from far field boundaries, T and F combine to oppose N . The maximum magnitude of N occurs at $x = L$ where another fault is most likely to develop. From equation (8), the maximum shear force on the vertical plane has following relationship:

$$N = \frac{1}{2} \mu_0 \rho g H^2 + \frac{2\eta \dot{\varepsilon}_0 L}{m+1} \leq \frac{1}{2} \mu_1 \rho g H^2 \quad (10)$$

where μ_1 is the frictional coefficient of intact rocks surrounding the master fault. The equation (10) can be further reduced to

$$L \leq \frac{(m+1) \Delta \mu \rho g H^2}{4 \dot{\varepsilon}_0 \eta} \quad (11)$$

where $\Delta \mu = \mu_1 - \mu_0$ is the strength contrast between a fault and surrounding rocks. Equation (11) relates the fault spacing to several physical parameters. Increasing brittle-layer thickness, H , strength contrast between faults and country rocks, $\Delta \mu$, or decreasing lower layer viscosity, η , and background strain rate, $\dot{\varepsilon}_0$, raises fault spacing. Increasing the power-law exponent, m , in equation (6) implies larger fault space, provided m is independent (or weakly dependent) on L . The effect of m is discussed in the next section. Additionally, the strength contrast $\Delta \mu$ should be the effective frictional coefficient difference between faults and intact rocks, which may be reduced in magnitude due to pore fluids in the gouge layer (Hickman, 1991).

2.2. Viscous deformation in lower layer

In the force balance analysis, shear strain rate at the top of a viscous layer is assumed to decrease away from driving faults following a power law. To establish a more accurate description of this process, the physical model beneath a frictionally moving fault can be simplified to a viscous flow driven by the top velocity discontinuity and side walls (Fig. 1c).

We make a 2D simplification for the viscous deformation in the lower layer. We assume an infinite length fault without variations in slip along strike (y direction). The top boundary is controlled by a velocity discontinuity, mathematically represented by a step function (Fig. 1c). The origin of the coordinate system coincides with the velocity discontinuity at the top surface. Only the fault-parallel velocity component (V_y) is non-zero. The non-zero strain rates are

$$\dot{\varepsilon}_{xy} = \frac{1}{2} \frac{\partial V_y}{\partial x} \quad \text{and} \quad \dot{\varepsilon}_{zy} = \frac{1}{2} \frac{\partial V_y}{\partial z} \quad (12)$$

An equilibrium state of deviatoric stresses occurs through a balance between shear stresses on vertical planes (zy), σ_{xy} , and on horizontal planes (xy), σ_{zy} (Fig. 1d):

$$\frac{\partial \sigma_{xy}}{\partial x} + \frac{\partial \sigma_{zy}}{\partial z} = 0 \quad (13)$$

With a Newtonian fluid of viscosity η , we have the constitutive relation:

$$\sigma_{ij} = 2\eta \dot{\varepsilon}_{ij} \quad (14)$$

Combining equations (12)–(14) yields a Laplace equation:

$$\frac{\partial^2 V_y}{\partial x^2} + \frac{\partial^2 V_y}{\partial z^2} = 0 \quad (15)$$

As the top velocity is applied in the form of a step function, the solution of equation (15) can be represented by a Fourier series combined with a linear function (Schrank, 2009):

$$V_y(x, z) = -\frac{V_0 x}{L} + \frac{V_0}{2} + \sum_1^{\infty} A_n(z) \sin\left(\frac{2\pi n x}{L}\right) \quad (16)$$

Equation (16) implies no-slip conditions at side walls. An additional constraint is to apply a zero-shear traction boundary condition at the base ($z = D$):

$$\frac{\partial V_y}{\partial z} = 0, \quad (17)$$

letting $k = \frac{2\pi n}{L}$, the desired amplitude spectrum $A_n(z)$ takes this form

$$A_n(z) = \frac{-\frac{V_0}{\pi n}}{e^{kD} + e^{-kD}} [e^{-kD} e^{kz} + e^{kD} e^{-kz}] \quad (18)$$

With equations (12) and (14), shear stress σ_{zy} has the following relationship:

$$\sigma_{zy}(x, z) = \eta \sum_1^{\infty} \frac{-\frac{V_0}{L}}{e^{kD} + e^{-kD}} [e^{-kD} e^{kz} - e^{kD} e^{-kz}] \sin(kx) \quad (19)$$

Integration of σ_{zy} in x gives the magnitude of the tangential tractions in the y direction as

$$F = \int_0^x \sigma_{zy} dx = \eta \sum_1^{\infty} \frac{-\frac{V_0}{2\pi n}}{e^{kD} + e^{-kD}} [e^{-kD} e^{kz} - e^{kD} e^{-kz}] [\cos(kx) - 1] \quad (20)$$

Alternatively, if the bottom boundary condition is changed to be a linear velocity

$$V_y(x, D) = -\frac{V_0 x}{L} + \frac{V_0}{2} \quad (21)$$

$A_n(z)$ in equation (16) takes form

$$A_n(z) = \frac{-\frac{V_0}{\pi n}}{e^{-kD} - e^{kD}} [(1 + e^{kD}) e^{kz} - e^{kD} e^{-kz}] \quad (22)$$

From equations (12) and (14), the stress σ_{zy} follows

$$\sigma_{zy}(x, z) = \eta \sum_1^{\infty} \frac{-\frac{V_0}{L}}{e^{-kD} - e^{kD}} [(1 + e^{kD}) e^{kz} + e^{kD} e^{-kz}] \sin(kx) \quad (23)$$

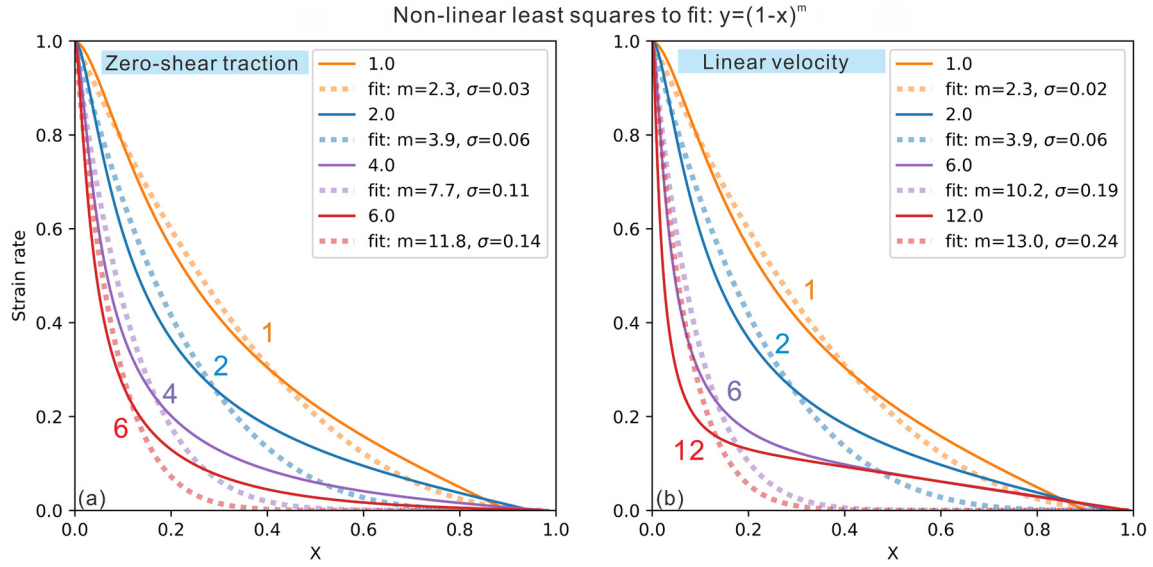


Fig. 2. Calibrating power-law exponent, m , in equation (6) with Fourier series solutions, using zero-shear traction (a) and linear-velocity (b) boundary conditions, respectively. The non-linear least square method is used to fit function $y = (1-x)^m$, where x , y are normalized distance and strain rate to corresponding maximum values. Colorful solid lines represent Fourier series solutions while the corresponding dashed lines are fitting results. The numbers near lines indicate the ratio of L/D .

Integration of σ_{zy} in x gives the magnitude of tangential tractions in the y direction as

$$F = \int_0^x \sigma_{zy} dx$$

$$= \eta \sum_1^{\infty} \frac{\frac{V_0}{2\pi n}}{e^{-kD} - e^{kD}} [(1 + e^{kD})e^{kz} + e^{kD}e^{-kz}] [\cos(kx) - 1]$$
(24)

Replacing equation (7) with equation (20) or (24), and performing the same analysis as equation (9), we find the relationship between fault spacing and other parameters:

$$f(L/D) \leq \frac{\Delta\mu\rho gH^2}{2V_0\eta}$$
(25)

where f is a function of L/D , which can be obtained by removing constant terms of V_0 and η in equation (20) or (24). The relationship between L and H can be illustrated by plotting L versus H in one figure with variations either in lower crust viscosity, η , strength contrast, $\Delta\mu$, or thickness of viscous layer, D .

To avoid the stress singularity associated with the step-function velocity boundary condition in analytical solutions, Savage and Lachenbruch (2003) introduced a pervasive Coulomb failure surrounding the singularity with a finite radius (r_0), which is far smaller than the brittle-layer thickness (H). Since the viscous stress decreases with distances from the origin point ($x = 0$, $z = H$) and the brittle strength increases with depth, the thicker the H , the smaller the r_0 of the region where brittle-viscous transition occurs. Lachenbruch and Sass (1992) simplified this analysis by considering a finite fault width (z_0) and selecting the depth at $z_0/2$ beneath the originally assumed brittle layer bottom as the new interface marking the top of a viscous layer. We take the approach of studying a range of possible fault widths.

The conventional idea of a fault zone width arises from the highly damaged zone associated with SAF, part of which is 100s-meter wide containing fault gouge (0.1–10s meters wide) (Chester et al., 1993). The phyllosilicate-rich (strain hardening material) Carboneras fault zone in the southeastern Spain is reported to be ~ 1 km in width (Faulkner et al., 2003). Alternative results reported

from seismologic observations suggest that the ~ 200 – 250 -meter wide damage zone extends to several kilometers in depth (Li et al., 2014). In our analysis, a 200-meter-wide fault zone, thus observing at 100 meters beneath the original interface, is set as a reference value in this study.

3. Model results and analysis

3.1. Calibrating power-law exponent, m , in equation (6)

The unknown power-law exponent, m , can be determined by fitting equation (19) or (23) with equation (6). Removing the constant viscosity term η in equation (19) or (23) produces the functional form of strain rate that is directly comparable with equation (6). The power-law exponent, m , is positively correlated to the aspect ratio, L/D (Fig. 2). When $L/D \leq 2$, fittings for different boundary conditions yield no significant difference in m . Additionally, the standard deviation of the fit increases with L/D , indicating that, with large L/D , the power-law decay in strain rate with distance from an active fault may not be a suitable approximation. For $L/D > 2$, power-law function shows slower decay in near field and faster decay in far field than that from the Laplace solutions. For a smaller aspect ratio ($L/D \leq 2$), the range of m is roughly 2–4. For natural cases, if the viscous lower layer is ~ 20 km and fault spacing is < 40 km, m of 2–4 may be used to estimate spatial distribution of strain rate. In the following discussions we assume Fourier series solutions for more accurate scaling of fault spacing.

3.2. Comparing models of two different boundary conditions

To investigate the effects of different boundary conditions, profiles of surface velocity, V_y , strain rate, $\dot{\epsilon}_{zy}$, and basal shear force, F , are shown in Fig. 3. All else being equal, increasing the aspect ratio L/D gives rise to steep velocity gradients across the dislocation center and corresponding high basal shear forces.

For the zero-shear-traction model, an upper limit in integrated basal forces exists for models of different aspect ratios. The basal traction tends to be asymptotic to a maximum value when $L/D \geq 4$ (Fig. 3c). By contrast, for the case with a linearly varying, prescribed velocity boundary condition, the asymptotic behavior is observed in the velocity distribution with depth when $L/D \leq 2$ (Fig. 4). For $L/2 \lesssim D$, the lateral velocity distribution does not vary

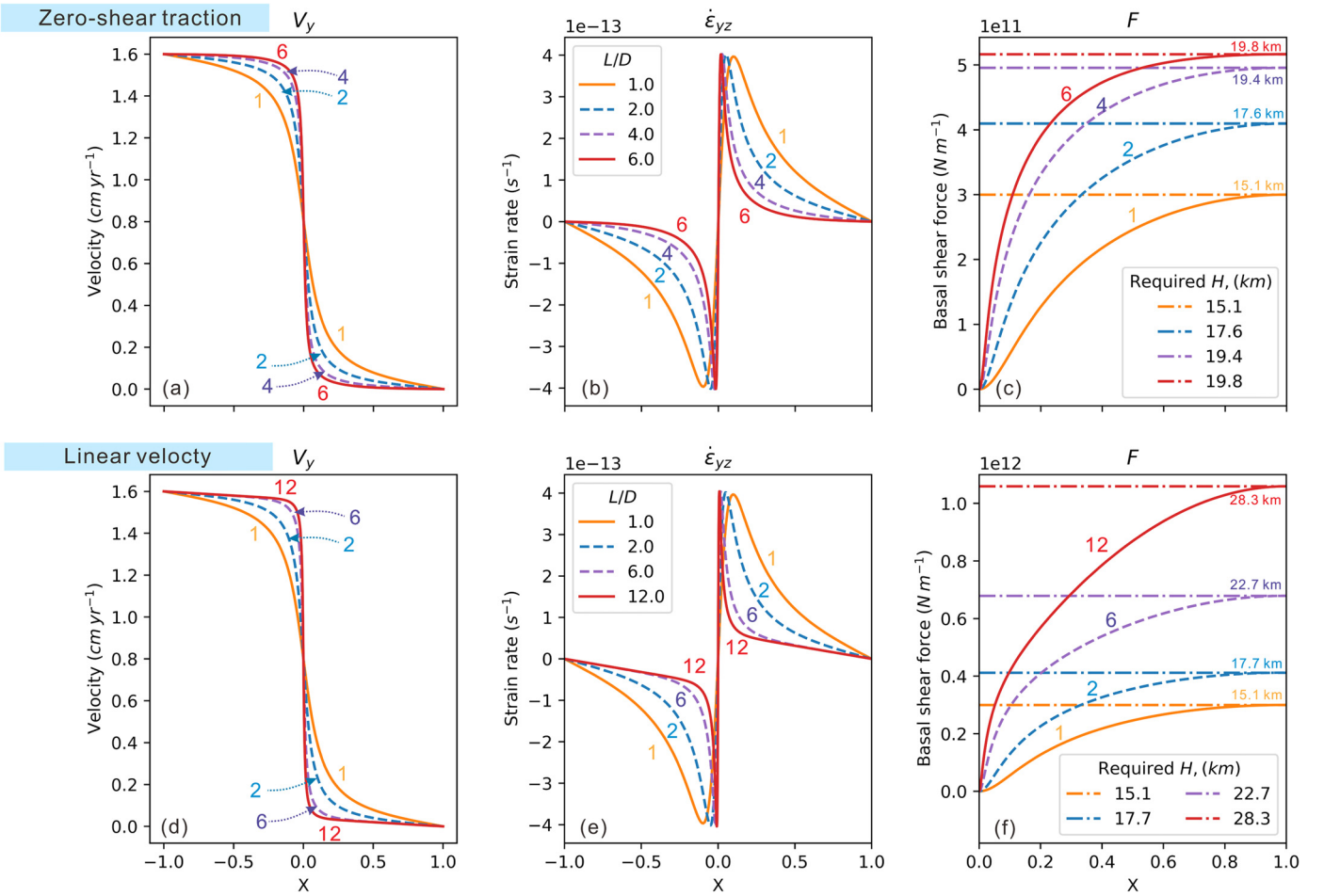


Fig. 3. Velocity, shear strain rate, and integrated shear force from models of different L/D for two different boundary conditions, zero-shear traction (a-c) and linear velocity (d-f). Distances are normalized to the corresponding model length L . Integrated force is calculated by an assumed viscosity of 10^{21} Pa-s. The horizontal lines plot in (c) and (f) are the required brittle-layer thickness to support basal shear forces. This calculation follows equation (25) with the assumed $\Delta\mu$, g and ρ to be 0.1 , 9.8 ms^{-2} , and 2700 kg m^{-3} , respectively. For the zero-shear case of $L/D = 1, 2, 4$ and 6 , the cutoff n for each case is $100, 220, 390$ and 480 , respectively. In the case of a linear velocity boundary condition, the selected n is $110, 220, 600$ and 1200 for $L/D = 1, 2, 6$ and 12 , respectively.

with depth, when the depth is larger than $L/2$. When $L/D \leq 2$, the velocity field at depth larger than $L/2$ is close to the linearly prescribed velocity in equation (21) (Fig. 4b), and the integrated basal traction is found to be two orders of magnitude smaller than the value at the top (Fig. 4a, b), which is effectively a zero basal shear force as equation (17). Therefore, for smaller L , the results from both cases are comparable.

The effect of boundary conditions can also be investigated by comparing basal shear force in Fig. 2d and Fig. 2f, where models with $L/D \leq 2$ demonstrate close values in terms of basal force and the required brittle-layer thickness to balance the force as is assessed by equation (9). With $L/D = 6$, the model with a linear-velocity boundary condition produces higher basal shear forces (6.7×10^{11} Nm^{-1}) than that of zero-shear boundary condition (5.1×10^{11} Nm^{-1}). The required brittle-layer thickness also increases from 19.8 km (zero-shear) to 22.7 km (linear-velocity).

For both cases, a thinner viscous layer (larger L/D) increases velocity gradients with depth, resulting in an increased integrated-basal-shear force and potentially reducing fault spacings. However, there is a limit for either effect of a viscous layer thickness. For a fixed L in a zero-shear model, reducing D to $< L/4$ does not result in any further changes to the basal shear force (Fig. 3c). In the linear-velocity model, increasing D to $> L/2$ produces no change in the velocity distribution beyond a depth of $L/2$ (Fig. 4b). The overall pattern can be summarized as follows: (1) the zero-shear case predicts that fault spacing should decrease with decreasing crustal

thickness until a threshold value is reached, below which fault spacing does not decrease significantly; (2) the linear-velocity case suggests that fault spacing should increase with increasing crustal thickness until another threshold value, above which fault spacing does not further increase. The threshold limit of either case is important in understanding coupling state between vertical layers.

4. Continental strike-slip faults

We compare our scaling law with empirical data from two inter-plate transform fault systems (SAF system in California and MFZ in New Zealand) and one intracontinental shear zone (the V-shaped shear zone from central Tibet). The SAF translates the total motion of ca. 48 mm yr^{-1} between the Pacific plate and the North American plate across an area of >300 km in width (Platt and Becker, 2010). The Marlborough Fault Zone (MFZ) is the northeast branch of the Alpine fault system, which accommodates ~ 38 mm yr^{-1} displacement between the Pacific and the Australian plate (Wallace et al., 2007). The along-strike (N110°E) slip rate in central Tibet is $5\text{--}10$ mm yr^{-1} (Yin and Taylor, 2011).

4.1. Fault spacing measurement

The fault spacing data in California is derived from Zuza et al. (2017) which includes shear zones in the Eastern Transverse Range (ETR, 20 ± 8 km) and Central California (CC, 33 ± 3 km), Western

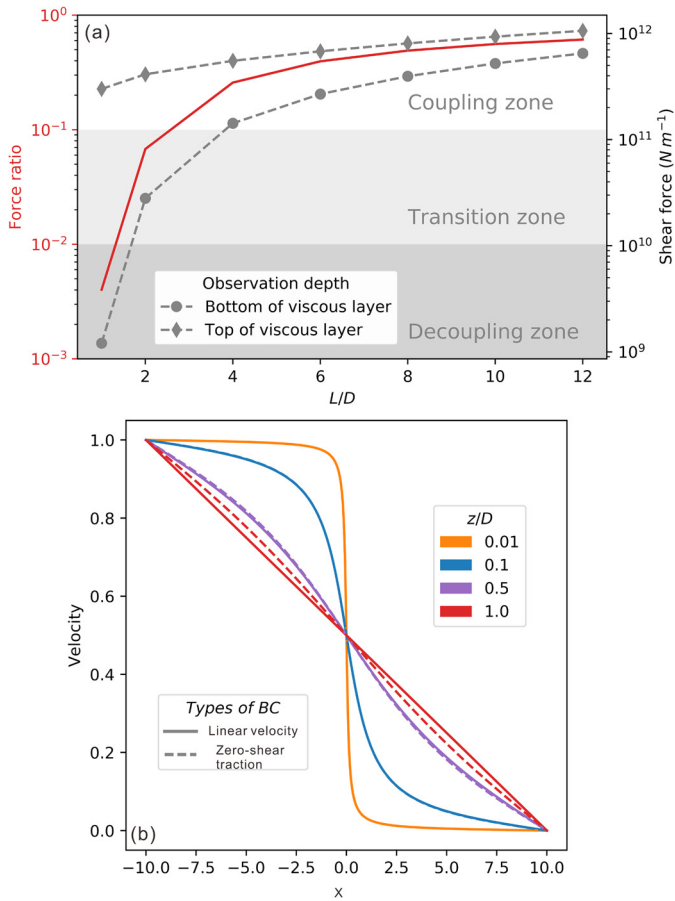


Fig. 4. (a) Integrated shear forces observed at both top and bottom (gray dashed line) versus L/D in a viscous layer with a prescribed linear velocity boundary condition. The red line shows ratios of the bottom force over the top force. When L/D is 4, the bottom force is about one fifth in magnitude of the top one. When the force ratio indicates over two orders of magnitude differences, this domain is suggested to be a decoupling zone. The force ratio of two to one order of differences in magnitude is a transition zone and that less than one order of magnitude is assigned to be a coupling zone. The decoupling zone means the basal drag has no significant control on top stress distributions. If L is fixed, increasing lower crust thickness tends to reduce the role of basal drag. (b) Comparing velocity distribution for two cases with $L/D = 2$. Different boundary conditions produce comparable velocity field in the upper half of the model domain. (For interpretation of the colors in the figure(s), the reader is referred to the web version of this article.)

Southern California (WSC, 47 ± 15 km) and Mojave (Mj, 16 ± 2 km) (Fig. 5a). Recent fault spacing measurements across Northern and Central Walker Lane (NWL) by Zusa and Carlson (2018) are included as well. The spacing data in central Tibet (CTb, 92 ± 24 km, Fig. 5b) also come from the compilation of Zusa et al. (2017). In addition, we compile fault spacing data from Southern Walker Lane (SWL, Fig. 5a) and the Marlborough Fault Zone (MFZ, Fig. 5c). SWL includes a complex array of normal faults and numerous minor strike-slip faults. We use the locations of major strike-slip faults based on the WGCEP (2007 Working group on California Earthquake Probabilities) fault traces. The long-term average strain rate of the selected major fault traces are orders of magnitude higher than that of less deformed areas (Bird, 2009) (Fig. 5a).

The fault spacing is measured by nearest-neighbor-fault distances perpendicular to average fault strike (Fig. 5). We sampled the spacing between adjacent faults at ~ 10 km along-strike increments; 8 measurements were compiled for two neighboring faults (Fig. S1). In that, 16 and 24 measurements yield a mean fault spacing value with standard deviations for SWL (three faults) and the MFZ (four faults), respectively (Table 1). We determine an average fault spacing of 47 ± 9 km for the three major faults comprising

the Southern Walker Lane Shear Zone (Fig. 5a): Owens Valley fault, Saline-Panamint Valley fault, and Furnace Creek-Death Valley fault, from west to east. The New Zealand Active Faults Database (GNS, <https://data.gns.cri.nz/af/>) is utilized to extract distance information for four major faults in the MFZ (Fig. 5c): Wairau, Awatere, Clarence, and Hope faults, from northwest to southeast, using the measurement increments (10 km) described above. The dominating dextral slip faults are oriented nearly parallel to relative motion between the Pacific plate and Australian plate. Regional geodetic observations suggest the ratio of strike-slip to dip-slip rate is $>6:1$ (Wallace et al., 2007). The average fault spacing in the MFZ is 23 ± 10 km, but the spacing between the Wairau and Awatere faults is 37 ± 4 km, which is about twice the averaged spacing for that between the Awatere and Clarence faults (17 ± 2 km), and between the Clarence and Hope faults (15 ± 3 km) (Fig. S1).

4.2. Brittle-layer thickness measurement

The brittle-layer thickness defined in our model can be approximated as equivalent to the thickness of the seismogenic layer in the crust. Most of the thickness data come from Zusa et al. (2017) and Zusa and Carlson (2018). We conduct our own seismogenic thickness measurement in SWL and the MFZ, which is not included in the Zusa database. Additionally, we update the seismogenic thickness in CTb with most recently published relocated hypocenters in CTb (Zhu et al., 2017). More than 400 relocated earthquakes recorded from 2013 to 2015 are used here to evaluate seismogenic thickness. The vertical uncertainty is about 0.9 km, which is obtained by comparing relocations with the actual locations of active seismic experiments (Zhou et al., 2019).

The brittle-layer thickness in California is calculated by using depth distributions of magnitude ≥ 3.0 earthquakes as a proxy for seismogenic thickness (data from the Southern California Earthquake Data Center) (Hauksson et al., 2012). The refined hypocenter depth uncertainty is reported to be less than 1.25 km, at 90% confidence. Earthquakes recorded during 2001–2010 in the MFZ are relocated with a national 3-D seismic velocity model (Eberhart-Phillips et al., 2005). The selected earthquakes in the MFZ have average standard errors of 0.5 km laterally and 0.7 km in depth. Selected hypocenters (1648 events) are projected to the profile itself (Fig. 5d). For the seismogenic thickness calculation of a chosen cross-section, data along the profile are divided into segments of a uniform length of 25 km. For each segment, the seismogenic thickness is defined as a depth, above which 95% of the events are located. This corresponding depth is marked as D95. We also demonstrate D95 for the total events along the entire profile (Fig. 5d & S2). The geometrical information used in this study is listed in Table 1.

Note that the brittle-ductile interface assumed in our model is a simplification of what is more likely a diffuse transition zone from brittle to semi-brittle deformation in nature. The end-member case in nature that is represented by our model may be faulting above a flowing salt layer. Small earthquakes can also happen in the transition zone of semi-brittle rheology, which has been the focus of recent slow-earthquake mechanics studies (Burgmann, 2018; Yin et al., 2018). Therefore, the D95 might have included both the brittle layer and transition zone. Since the transition zone strength is generally weaker than the brittle strength at the same depth, the estimated frictional strength should be the lower limit of the pure brittle fault strength. It depends on the proportion of the transition zone thickness in the D95. The lower the proportion, the estimated fault strength closer to the pure brittle friction strength.

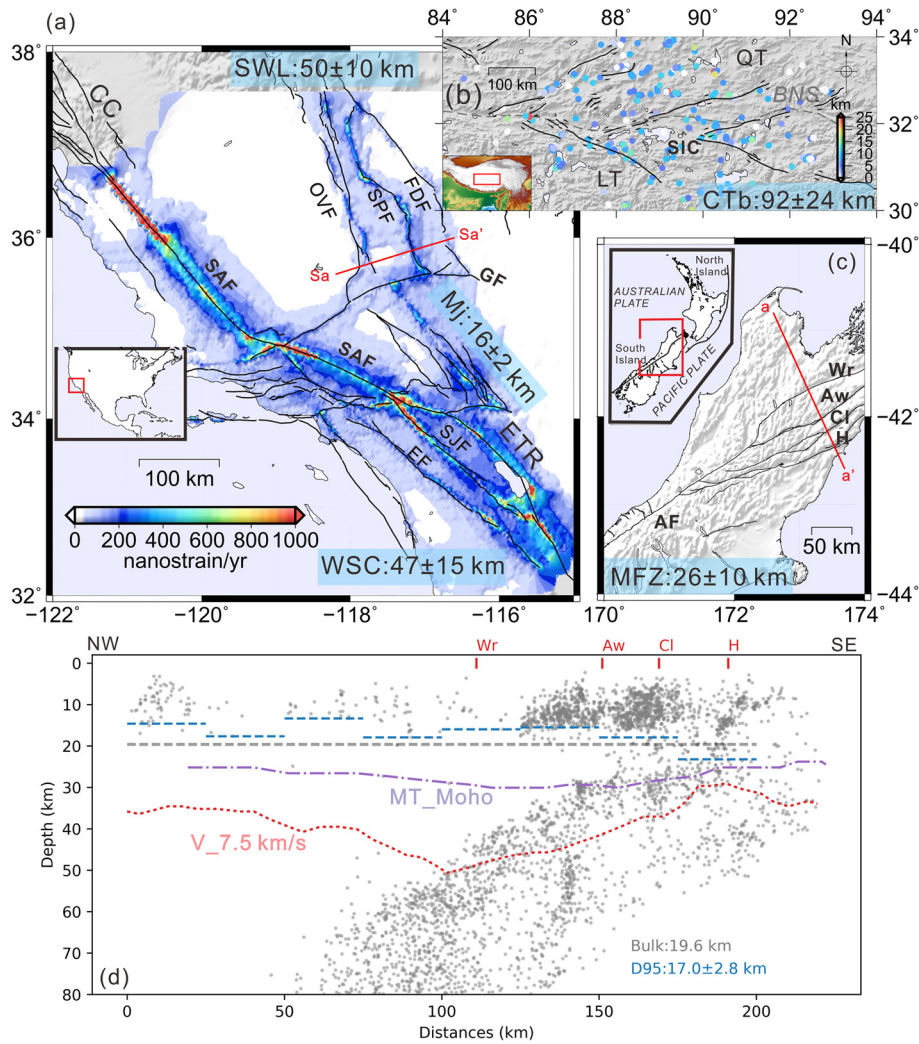


Fig. 5. Simplified tectonic maps showing evenly spaced faults (thin black lines) in California (a), central Tibet (b), and New Zealand (c). (a) Color map is the long-term-averaged strain rate in California (Bird, 2009). Western Southern California (WSC) includes San Andreas fault (SAF), San Jacinto fault (SJF), Elsinore fault (EF); Southern Walker Lane Shear Zone (SWL) are composed of major faults of Owens Valley fault (OVF), Saline-Panamint Valley fault (SPF) and Furnace Creek-Death Valley fault (FDF). Other study areas shown here are Eastern Transverse Range (ETR) and Central California (CC). (b) The V-shaped strike-slip faults in central Tibet locates across the Bangong-Nujinag suture (BNS), which separates the Qiangtang terrane (QT) and Lhasa terrane (LT). SIC stands for the lake Siling Co. Regional earthquakes are plot with colorful dots to indicate focal depths. (c) The Marlborough Fault Zone (MFZ) is the north branch of the Alpine Fault (AF). Only dextral fault with slip rate $>1 \text{ mm yr}^{-1}$ are selected here. Major faults include Wairau fault (Wr), Awatere fault (Aw), Clarence fault (Cl) and Hope fault (H). Numbers in cyan-faced boxes indicate fault spacing in corresponding areas. Red-straight lines show selected cross-sections to investigate regional brittle-layer thickness. Hypocenters on each profile are projected from those within $\pm 80 \text{ km}$ distances. (d) Cross-section (the red line aa' in c) of focal depth distribution in MFZ. The profile is divided into uniform lengths of 25 km. The cutoff depth is set by counting earthquakes above which 95% (D95) earthquakes are contained. The red dot line is an iso-velocity contour of 7.5 km s^{-1} , which is suggested to be an approximation of the velocity gradient at the Moho (Eberhart-Phillips and Bannister, 2010) and the purple dash-dotted line is the interpreted Moho depth from the magnetotelluric (MT) sounding, which is located parallel to and about 40 km to south of the selected profile (Wannamaker et al., 2009). Earthquakes in SWL (a) are projected to the red profile (SaSa') and those in central Tibet is project to the 32°N latitude line (see supplementary material).

Table 1
Fault spacing and seismogenic thickness.

	D95 thickness (km)	Fault spacing (km)
Mojave ^a (Mj)	11.9 ± 1.1	16 ± 2
Western Southern California ^a (WSC)	15.7 ± 1.1	47 ± 15
Southern Walker Lane	10.6 ± 1.4	47 ± 9
Eastern Transverse Range ^a (ETR)	12.1 ± 1.5	20 ± 8
Central California ^a (CC)	14.4 ± 1.9	33 ± 3
Marlborough Fault Zone (MFZ)	17.0 ± 2.8	23 ± 10
Central Tibet (CTb)	14.1 ± 2.2	92 ± 24
Northern and Central Walker Lane ^a (NWL)	14.3 ± 1.4	15 ± 5
	10.5 ± 0.6	12 ± 2
	9.6 ± 1.9	10 ± 3
	11.2 ± 0.7	14 ± 4

^a Data of fault spacing and brittle layer thickness come from Zuza et al. (2017) and Zuza and Carlson (2018). NWL includes four shear zone: Pyramid Lake domain, Carson domain, Walker Lake Domain, and Mina Deflection, respectively.

5. Discussion

5.1. Relationship between L , H , η , $\Delta\mu$, and V_0

The compiled data of fault spacing versus brittle-layer thickness ($L - H$) are shown in Fig. 6 with contours showing how different viscosities and strength contrast affect the $L - H$ slope. The contours are plotted following equation (25). L is proportional to H positively and related to η negatively (Fig. 6). The positive-correlation relationship also holds for L versus $\Delta\mu$ (Fig. 6). Conclusions derived from equation (6) does not change. The relationship among L , H and $\Delta\mu$ is consistent with studies of Roy and Royden (2000a). Shallower faults in the early stage of deformation are expected to have closer distances than those in later stages, when they cut deeper. The viscoelastic models in Roy and Royden (2000b) demonstrate that faults evolve by cutting

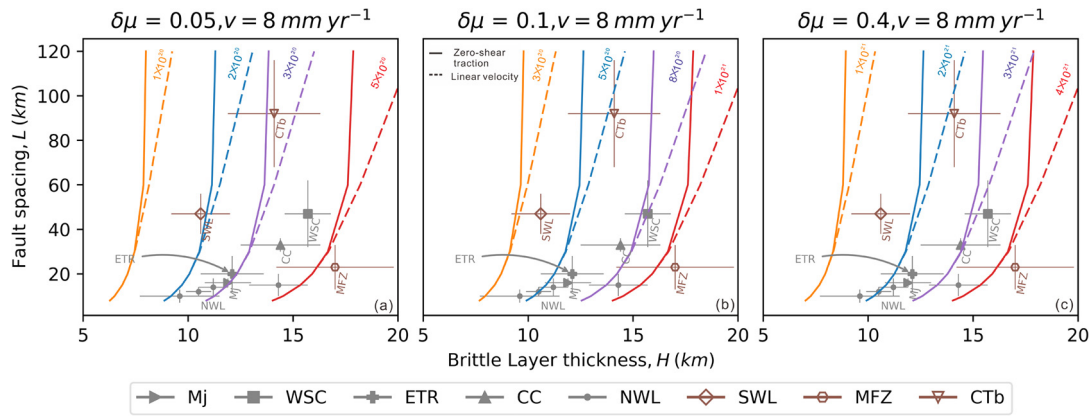


Fig. 6. Fault spacing versus brittle-layer thickness with viscosity contours (unit: Pa·s) at slip rate of 8 mm yr^{-1} for $\Delta\mu = 0.05$ (a), 0.1 (b) and 0.4 (c). Markers show compiled data from the SAF system, MFZ and CTb. Solid gray markers come from Zuza et al. (2017) and Zuza and Carlson (2018). Non-filling markers are compiled by this study. The theoretical calculations are processed under the same assumption of a viscous layer thickness, D , gravity accelerate, g , and upper layer density, ρ , to be 15 km , 9.8 m s^{-2} , and 2700 kg m^{-3} , respectively.

deeper and deeper, thus increasing fault spacing. Roy and Royden (2000b) pointed that crust with similar fracture strength (intact material) and failure strength (reactivated faults) tends to produce much smaller fault spacing than would occur with a greater strength contrast. On the other hand, a mature fault is conventionally thought to form through coalescing cracks and smoothing geometrical asperities, thus further weakening its strength (Wesnousky et al., 1983). Since reducing a fault strength increases the strength contrast between a fault and surrounding rocks, the weakening process also contributes to growing fault spacing. From the perspective of a fault evolution, fault spacing increases over time with increasing H and $\Delta\mu$.

In the compiled data from the SAF system (gray filled markers in Fig. 6), there is a clear trend showing a positive relationship between brittle-layer thickness and fault spacing, except one point from Northern and Central Walker Lane (NWL). With the assumption of a linear relationship between L and H , two lines with different slopes to are required to fit data in California and Walker Lane (Zuza and Carlson, 2018). With our non-linear scaling of $L - H$, the slope slowly increases with H until reaching one threshold value (e.g. $L \approx 30 \text{ km}$ in Fig. 6), beyond which it approximates a linear trend with the steepest L/H slope. In this case, a linear trend in regions with small fault spacing ($< 30 \text{ km}$) may be a simplified approximation. Such characteristic spacing value ($\sim 30 \text{ km}$) is about twice the viscous layer thickness (15 km). The analogue modeling in Zuza et al. (2017) shows that when $h \sim 3-4 \text{ cm}$, the fault spacing is higher than the prediction from a linear trend (see Fig. 4e in Zuza et al., 2017), permitting a nonlinear scaling of $L - H$. This phenomenon is consistent with our scaling of $L - H$. Note that the zero-shear case shows much steeper slope than the linear-velocity one when brittle layer is thick enough. This is attributed to the fact that increasing $L/D \geq 4$ does not increase basal shear force so significantly that the calculated brittle-layer required to support the basal traction does not vary significantly (Fig. 3c). The steep slope in the model with no-shear boundary condition does not appear in the case with linear-velocity boundary condition (Fig. 6), because there is not upper limit of basal shear force with increasing L/D , as is demonstrated in Fig. 3f.

Comparing theoretical values of $L - H$ with contours of viscosity, we can use field observations to constrain viscosity values in the viscous lower layer. With equation (25), given the knowledge of geometrical parameters, L , H and D , it is the ratio of $\Delta\mu/V_0$ that determines the solution of viscosity. Increasing $\Delta\mu$ or decreasing V_0 has same effect in controlling fault spacing, and synchronously doubling values of $\Delta\mu$ and V_0 does not alter the estimation of viscosity. For short-term dynamics of earthquake rupture

propagations (e.g. the state-and-rate friction), $\Delta\mu$ is positively related to V_0 (Scholz, 1998). For the long-term case, a mature major fault in one fault system is also taken as the weakest one (large $\Delta\mu$) such that it has the fastest dislocation rate, like SAF comparing with faults in Mojave (Wesnousky et al., 1983). As there is a large variation of slip rate for each fault in one shear zone, and even the estimation of slip rate of one fault can vary significantly by different methods (Petersen and Wesnousky, 1994), recent databases may not be sufficient for working out the effect of fault slip rate. We simply combine the effect of $\Delta\mu$ and V_0 to $\Delta\mu$, and investigate its control on the solution of lower layer viscosity with a constant V_0 (Fig. 6). Possible ranges of $\Delta\mu$ and V_0 are given to evaluate corresponding viscosities. The effective viscosity of the viscous layer underlying the brittle layer for all the compiled data from different tectonic settings is $2 \times 10^{20} - 4 \times 10^{21} \text{ Pa}\cdot\text{s}$ (Fig. 6).

Although data compiled from Zuza shows a positive correlation between L and H , it is clear the ratios of L/H vary in different tectonic settings. The brittle-layer thickness or D95 depth does not vary that much globally (brittle-layer thickness might vary 5 to 25 km in general), but fault spacing clearly varies much more significantly, from kilometers in SAF to $> 500 \text{ km}$ in central Asia. In the SAF system, SWL shows brittle thickness close to that in Mojave, but the fault spacing is more than 3 times higher. The brittle-layer thickness in the MFZ is comparable with that in Western Southern California (WSC), but the fault spacing is only half of that in WSC. These exceptional patterns may be attributed to specific physical conditions in the viscous lower layer.

5.2. Lower crust viscosity in Southern Walker Lane

Fig. 6 suggests that the effective viscosity in the lower crust beneath Southern Walker Lane (SWL) is $2 \times 10^{20} - 2 \times 10^{21} \text{ Pa}\cdot\text{s}$, which is lower than that in Mojave. The low viscosity in SWL is also demonstrated by Shinevar et al. (2018). Without considering hydrous phases and melt effect, the estimated aggregate viscosity from Shinevar et al. (2018) in southeastern Sierra Nevada at 25 km depth is around $10^{22} \text{ Pa}\cdot\text{s}$, which thus represents an upper bound. This lower viscosity in SWL may be attributed to high background heat flow ($> 250 \text{ mW m}^{-2}$), close to the Coso Geothermal field in the southeastern Sierra Nevada. Heat flow in other study areas in Southern California are $60-100 \text{ mW m}^{-2}$ (<https://geomaps.wr.usgs.gov/heatflow/index.htm>). This indicates much higher crustal temperature in the SWL than that in WSC and Mojave. Based on the heat flow measurement from Williams and DeAngelo (2011) and SMU Geothermal Database (<http://geothermal.smu.edu/gtda/>), Shinevar et al. (2018) obtained crustal temperature in Southern

California and found that temperature at depth 25 km in SWL is over 100°C higher than that in Mojave. Additionally, seismic imagings have found that the hot area in the southeastern Sierra Nevada lost its crustal root (Jones et al., 1994; Fliedner et al., 1996). Following the delamination, pulsive emplacement of mafic potassic magmatism was recorded ca. 3.5 Ma (Manley et al., 2000). These might have led to high heat flow in SWL.

5.3. Lower layer viscosity in Central Tibet

Consistent with the reasoning for wider spacing in SWL, we attribute the wider fault spacing in Central Tibet (CTb) to the layer of a relatively lower viscosity underlying the brittle layer. All else being equal, $L-H$ data with contours of viscosity in Fig. 6 suggest the viscosity of CTb (3×10^{20} – 3×10^{21} Pa·s) is lower than those in the Western United States (gray filled markers in Fig. 6), but not lower than that in SWL. Two reliable heat flow measurements are 46.7 mWm⁻² in southern Qiangtang Terrane (He et al., 2014) and 140 mWm⁻² in northern Lhasa Terrane near the Bangong-Nujiang suture (Jiang et al., 2019). The wide range of heat flow in CTb overlaps with that in Western Southern California, but the upper bound is not as high as that in the SWL. That means the lower crust strength in CTb may not be as low as that in SWL. There is geomorphic proxy evidence suggesting a relatively weak lower crust of viscosity $\leq 10^{19}$ Pa·s beneath Siling Co (Fig. 5b) (Shi et al., 2015), which is located in the north of Lhasa Terrane and near the Bangong-Nujiang suture. This estimate is about one order of magnitude lower than our results. England and Walker (2016) commented on the assumption of a thick elastic lid (~20–30 km) overlying an inviscid lower crust in Shi et al. (2015) and provided an alternate estimate for the viscosity $> 5 \times 10^{19}$ – 2×10^{20} Pa·s assuming an elastic lid thickness less than 25 km. This agrees with our predictions of the middle-lower crust viscosity in CTb. Additionally, other studies from England et al. (2013) and Henriquet et al. (2019) also suggested the upper bound of the long-term viscosity in the middle to lower crust is $> 10^{20}$ Pa·s. The current state of such high viscosity is two orders of magnitude higher than the conditions to form “channel flow” tectonics, which is widely used to explain the morphology and structures in eastern Tibet and the Himalaya (Royden et al., 1997).

With determined geometrical parameters, L and H , a lower $\Delta\mu$ (or $\Delta\mu/V_0$) requires a weaker viscous layer than the case of higher values. If the true value of viscosity in CTb is close to the lower endmember, $\Delta\mu$ (or $\Delta\mu/V_0$) should be small as well. The lower $\Delta\mu$ means that fault strength in CTb is close to surrounding rocks, thus indicating a strong fault. A lower $\Delta\mu/V_0$ indicates that faults healing may dominate over strain weakening processes in CTb. The lower bound of our modeled viscosity ($\sim 10^{20}$ Pa·s) has significant overlaps with other studies. In this case, the strength contrast between faults and surrounding rocks is < 0.1 , which tends to produce diffusive brittle deformations in the shallow crust. This is consistent with epicenter distributions in CTb (Zhu et al., 2017).

5.4. Lower crust thickness and basal driving in the MFZ

With the assumption of $\Delta\mu$ ranging from 0.05 to 0.4 and lower crust thickness of 2 km (not the thickness value used in Fig. 6), the lower crust viscosity in the southeastern Marlborough Fault Zone (MFZ) is estimated to lie in the range 3×10^{20} – 3×10^{21} Pa·s. The narrow fault spacing in the MFZ relative to Western Southern California (WSC), occurs in an area with similarly thick brittle crust, suggesting that the reduced L in the MFZ does not reflect a lower value of H . The lower values of L relative to H in the MFZ could be explained by a higher viscosity as indicated in Fig. 6. High viscosity in the lower crust could originate from relatively low temperatures or predominance of mafic material. However, the

measured regional heat flow is 60–80 mWm⁻² (Shi et al., 1996) – close to that in WSC, suggesting temperature variations alone cannot explain differences in the value of L . Furthermore, no evidence exists to suggest a more felsic lower crust in WSC than that in the MFZ. A receiver function study in Southern California suggested a high V_p/V_s ratio of 1.8–1.85 in WSC, indicating a mafic lower crust there (Zhu and Kanamori, 2000). Seismic studies also indicate a mafic lower crust in the MFZ (Eberhart-Phillips and Bannister, 2010). Ruling out the possible effects of temperature and composition, we hypothesize that the difference in fault spacing between WSC and the MFZ may instead relate to variations in lower crust thickness and bottom boundary conditions.

Lower crust thickness is estimated by subtracting brittle thickness from total crust thickness. The crust in WSC is mapped to be 30–35 km thick (Zhu and Kanamori, 2000). With a ~15-km-thick brittle layer, the resulted lower crust is 15–20 km thick. The continental crust thickness in the MFZ is difficult to estimate using seismic data, as the lower crust beneath the eastern half of the MFZ is obliquely under-thrust by the Pacific, resulting in a weak seismic velocity difference across the Moho. Three fault-normal cross-sections of V_p and V_p/V_s extending from the north, middle and south of the MFZ all show similar geophysical anomalies (Eberhart-Phillips and Bannister, 2010), indicating minimal variations along fault-strike direction. Other geophysical profiles (Wannamaker et al., 2009) within 40 km of the selected red profile in Fig. 5c also sheds light on details of crustal structures. Combining results from velocity inversion considering seismic wave anisotropy (Eberhart-Phillips and Henderson, 2004) and lithospheric resistivity field obtained from a magnetotelluric survey, Wannamaker et al. (2009) indicated the top of the subducted Pacific plate (by proxy, base of the lower crust) is at a depth of ~25 km (Fig. 5). In this case, the lower crust in the eastern part of the MFZ is < 10 km thick – much thinner than that in WSC (15–20 km). Within the MFZ, there is a trend of increasing fault spacing from southeast (15 ± 3 km) to northwest (37 ± 4 km). This relationship may also be attributed to northward increasing lower crustal thickness, which increases from < 8 km beneath the Hope Fault to more than 25 km beneath Wairau and Awatere faults (Eberhart-Phillips and Bannister, 2010), which is also weakly coupled with the subducted Pacific plate.

5.5. Lower boundary condition

In our physical analysis, two end-member boundary conditions have been studied. The free-slip condition represents a weak lowermost crust or shallow mantle, which decouples the overlying crustal deformation from underlying dynamics of the mantle. The prescribed linear velocity condition is typical for cases of coupled deformation in both crust and mantle. The case of the approximately fixed linear velocity boundary condition may occur in the eastern MFZ where the lower crust is kinematically coupled to the subducted oceanic plate. The strong coupling is evidenced by observations of concurrent, triggered slip on crustal faults and the subduction interface during the 2016 Mw7.8 Kaikoura earthquake (Mouslopoulou et al., 2019). The surface rupture of the Kaikoura earthquake was proposed to be regulated by spatiotemporal patterns of megathrust locking in the eastern MFZ beneath the Clarence and Hope faults (Lamb et al., 2018), indicating a kinematically coupled motion for the crust and the under-thrusted oceanic plate. Increasing lower crust thickness may reduce the effect of bottom boundary condition for both cases. Our physical analysis suggests (Figs. 3 & 4), if $L/2 \leq D$, the effect of lower boundary condition on stress distribution on the brittle-ductile interface is negligible. The crust thickness in Southern California is 30–35 km (Zhu and Kanamori, 2000), the brittle-layer thickness is 10–15 km, and thus the implied lower-crust thickness is 15–25 km. With fault

spacing data in Southern California, the required minimum lower-crust thickness for the Mojave, Eastern Transverse Range, Central California, Western Southern California and Southern Walker Lane (SWL) are 8 km, 10 km, 16.5 km, 23.5 km and 23.5 km, respectively. This approximates the requirement for a free-slip boundary condition. The lower crust in SWL is not thick enough to decouple unless it is also weak in these regions and this is supported by the high heat flow.

6. Conclusions

We derive a scaling law for evenly-spaced faults in continental strike-slip shear zones using estimates of brittle-layer thickness, strength contrast between faults and their bounding intact rocks, and underlying-layer viscosity and thickness. Our model is based upon an assumption of long-term, on-going deformation in the crust in which the faults are frictionally sliding boundaries between relatively rigid blocks, which themselves induce flow in an underlying viscous layer. On the one hand, the thicker the brittle layer or the larger the strength contrast between faults and surrounding rocks, the greater the spacing to the neighboring fault. On the other hand, thinner lower crust or larger lower crust viscosity promotes smaller fault spacings. If the lower crust is thicker than half the fault spacing, the effect of basal drag on fault development is negligible. These are verified by data from shear zones in the SAF system, and the MFZ. In principle, with known structural parameters and better knowledge of fault strength, our model can predict an effective viscosity for the viscous layer underlying the brittle crust. The same approach can be applied in some other strike-slip shear zones to assess the regional rheological parameters, which is an important but not directly measurable unknown, inherent in earthquake studies.

Acknowledgements

We thank the Australian Research Council for funding this research under Discovery Grant DP170103350. Insightful suggestions from the editor Dr. Yin A., critical comments from Dr. Zuza A. and three other anonymous reviewers have greatly improved the clarity and focus of the work. Dr. Eberhart-Phillips provided relocated hypocenters in the MFZ. Dr. Zhou Beibei and Zhu Gaohua provided relocated hypocenters in CTb. Dr. Shinevar shared viscosity estimates in Southern California for comparison. We made use of resources from the National Computational Infrastructure (NCI), as well as the Pawsey Supercomputing Centre. H. Yang received the Baragwanath Travel Scholarship from the University of Melbourne to assist in research development. One figure in this paper was produced by using the Generic Mapping Tools (GMT) package (Wessel et al., 2013).

Appendix A. Supplementary material

Supplementary material related to this article can be found online at <https://doi.org/10.1016/j.epsl.2019.115906>.

References

Bird, P., 2009. Long-term fault slip rates, distributed deformation rates, and forecast of seismicity in the western United States from joint fitting of community geologic, geodetic, and stress direction data sets. *J. Geophys. Res., Solid Earth* 114. <https://doi.org/10.1029/2008JB006071>.

Burgmann, R., 2018. The geophysics, geology and mechanics of slow fault slip. *Earth Planet. Sci. Lett.* 495, 112–134. <https://doi.org/10.1016/j.epsl.2018.05.014>.

Chester, F.M., Evans, J.P., Biegel, R.L., 1993. Internal structure and weakening mechanisms of the San-Andreas fault. *J. Geophys. Res., Solid Earth* 98, 771–786. <https://doi.org/10.1029/1992JB007501>.

Eberhart-Phillips, D., Bannister, S., 2010. 3-D imaging of Marlborough, New Zealand, subducted plate and strike-slip fault systems. *Geophys. J. Int.* 182, 73–96. <https://doi.org/10.1111/j.1365-2466.2010.01827.x>.

Eberhart-Phillips, D., Henderson, C.M., 2004. Including anisotropy in 3-D velocity inversion and application to Marlborough, New Zealand. *Geophys. J. Int.* 156, 237–254. <https://doi.org/10.1111/j.1365-2466.2004.00987.x>.

Eberhart-Phillips, D., Reyners, M., Chadwick, M., Chiu, J.M., 2005. Crustal heterogeneity and subduction processes: 3-D Vp, Vp/Vs and Q in the southern North Island, New Zealand. *Geophys. J. Int.* 162, 270–288. <https://doi.org/10.1111/j.1365-2466.2004.00987.x>.

England, P., Walker, R.T., 2016. Comment on: “Crustal strength in central Tibet determined from Holocene shoreline deflection around Siling Co” by Xuhua Shi, Eric Kirby, Kevin P. Furlong, Kai Meng, Ruth Robinson and Erchie Wang. *Earth Planet. Sci. Lett.* 433, 393–395. <https://doi.org/10.1016/j.epsl.2016.05.014>.

England, P.C., Walker, R.T., Fu, B.H., Floyd, M.A., 2013. A bound on the viscosity of the Tibetan crust from the horizontality of palaeolake shorelines. *Earth Planet. Sci. Lett.* 375, 44–56. <https://doi.org/10.1016/j.epsl.2013.02.014>.

Faulkner, D.R., Lewis, A.C., Rutter, E.H., 2003. On the internal structure and mechanics of large strike-slip fault zones: field observations of the Carboneras fault in southeastern Spain. *Tectonophysics* 367, 235–251. [https://doi.org/10.1016/S0040-1075\(02\)00211-1](https://doi.org/10.1016/S0040-1075(02)00211-1).

Fliedner, M.M., Ruppert, S., Malin, P.E., Park, S.K., Jiracek, G., Phinney, R.A., Saleeby, J.B., Wernicke, B., Clayton, R., Keller, R., Miller, K., Jones, C., Luetgert, J.H., Mooney, W.D., Oliver, H., Klempner, S.L., Thompson, G.A., 1996. Three-dimensional crustal structure of the southern Sierra Nevada from seismic fan profiles and gravity modeling. *Geology* 24, 367–370. [https://doi.org/10.1130/S0092-7070\(1996\)024<0367:3DCS>2.0.CO;2](https://doi.org/10.1130/S0092-7070(1996)024<0367:3DCS>2.0.CO;2).

Hauksson, E., Yang, W.Z., Shearer, P.M., 2012. Waveform relocated earthquake catalog for Southern California (1981 to June 2011). *Bull. Seismol. Soc. Am.* 102, 2239–2244. <https://doi.org/10.1785/BSSA-102-05-02239>.

He, J.L., Wang, J., Tan, F.W., Chen, M., Li, Z.X., Sun, T., Wang, P.K., Du, B.W., Chen, W.B., 2014. A comparative study between present and palaeo-heat flow in the Qiangtang Basin, northern Tibet, China. *Mar. Pet. Geol.* 57, 345–358. <https://doi.org/10.1016/j.marpetgeo.2014.05.014>.

Henriquet, M., Avouac, J.P., Bills, B., 2019. Crustal rheology of southern Tibet constrained from lake-induced viscoelastic deformation. *Earth Planet. Sci. Lett.* 506, 308–322. <https://doi.org/10.1016/j.epsl.2019.02.014>.

Hickman, S.H., 1991. Stress in the lithosphere and the strength of active faults. *Rev. Geophys.* 29, 759–775. <https://doi.org/10.1029/1990RG000111>.

Jiang, G.Z., Hu, S.B., Shi, Y.Z., Zhang, C., Wang, Z.T., Hu, D., 2019. Terrestrial heat flow of continental China: updated dataset and tectonic implications. *Tectonophysics* 753, 36–48. <https://doi.org/10.1016/j.tecto.2019.05.014>.

Jones, C.H., Kanamori, H., Roecker, S.W., 1994. Missing roots and mantle “drips”: regional Pn and teleseismic arrival times in the southern Sierra Nevada and vicinity, California. *J. Geophys. Res., Solid Earth* 99, 4567–4601. <https://doi.org/10.1029/1993JB002011>.

Lachenbruch, A.H., Sass, J.H., 1992. Heat-flow from Cajon Pass, fault strength, and tectonic implications. *J. Geophys. Res., Solid Earth* 97, 4995–5015. <https://doi.org/10.1029/1991JB006071>.

Lamb, S., Arnold, R., Moore, J.D.P., 2018. Locking on a megathrust as a cause of distributed faulting and fault-jumping earthquakes. *Nat. Geosci.* 11, 871. <https://doi.org/10.1038/s41562-018-0414-1>.

Li, Y.G., De Pascale, G.P., Quigley, M.C., Gravelly, D.M., 2014. Fault damage zones of the M7.1 Darfield and M6.3 Christchurch earthquakes characterized by fault-zone trapped waves. *Tectonophysics* 618, 79–101. <https://doi.org/10.1016/j.tecto.2014.05.014>.

Manley, C.R., Glazner, A.F., Farmer, G.L., 2000. Timing of volcanism in the Sierra Nevada of California: evidence for Pliocene delamination of the batholithic root? *Geology* 28, 811–814. <https://doi.org/10.1130/G27099.1>.

Mouslopoulou, V., Saltogianni, V., Nicol, A., Oncken, O., Begg, J., Babeyko, A.Y., Cesca, S., Moreno, M., 2019. Breaking a subduction-termination from top to bottom: the large 2016 Kaikōura Earthquake, New Zealand. *Earth Planet. Sci. Lett.* 506, 221–230. <https://doi.org/10.1016/j.epsl.2019.02.014>.

Petersen, M.D., Wesnousky, S.G., 1994. Fault slip rates and earthquake histories for active faults in Southern California. *Bull. Seismol. Soc. Am.* 84 (5), 1608–1649. <https://doi.org/10.1785/BSSA-84-5-1608>.

Platt, J.P., Becker, T.W., 2010. Where is the real transform boundary in California? *Geochem. Geophys. Geosyst.* 11. <https://doi.org/10.1029/2009GC003611>.

Quigley, M., Karlstrom, K.E., Kelley, S.A., Heizler, M., Umhoefer, P., Beard, L.S., Lamb, M.A., 2010. Timing and mechanisms of basement uplift and exhumation in the Colorado Plateau-Basin and Range transition zone, Virgin Mountain anticline, Nevada-Arizona. In: *Miocene Tectonics of the Lake Mead Region, Central Basin and Range*. In: Geological Society of America Special Papers, vol. 463, pp. 311–329. <https://doi.org/10.1130/SPE517>.

Rolandone, F., Jaupart, C., 2002. The distributions of slip rate and ductile deformation in a strike-slip shear zone. *Geophys. J. Int.* 148, 179–192. <https://doi.org/10.1046/j.1365-2466.2002.0148179.x>.

Roy, M., Royden, L.H., 2000a. Crustal rheology and faulting at strike-slip plate boundaries: 1. An analytic model. *J. Geophys. Res., Solid Earth* 105, 5583–5597. <https://doi.org/10.1029/1999JB000001>.

Roy, M., Royden, L.H., 2000b. Crustal rheology and faulting at strike-slip plate boundaries: 2. Effects of lower crustal flow. *J. Geophys. Res., Solid Earth* 105, 5599–5613. <https://doi.org/10.1029/1999JB000002>.

Royden, L.H., Burchfiel, B.C., King, R.W., Wang, E., Chen, Z., Shen, F., Liu, Y., 1997. Surface deformation and lower crustal flow in Eastern Tibet. *Science* 276, 788–790. <https://doi.org/10.1126/science.276.5317.788>.

Savage, J.C., Lachenbruch, A.H., 2003. Consequences of viscous drag beneath a transform fault. *J. Geophys. Res., Solid Earth* 108. <https://doi.org/10.1029/2002JB001801>.

Scholz, C.H., 1998. Earthquakes and friction laws. *Nature* 391, 37–42. <https://doi.org/10.1038/391037a>.

Schrank, C.E., 2009. Physical Models of Shear Zones: on the Relationship Between Material Properties and Shear Zone Geometry (PhD diss.). <https://doi.org/10.1029/2009GC003611>.

Shi, Y.L., Allis, R., Davey, F., 1996. Thermal modeling of the Southern Alps, New Zealand. *Pure Appl. Geophys.* 146, 469–501. <https://doi.org/10.1007/BF00602411>.

Shi, X.H., Kirby, E., Furlong, K.P., Meng, K., Robinson, R., Wang, E., 2015. Crustal strength in central Tibet determined from Holocene shoreline deflection around Siling Co. *Earth Planet. Sci. Lett.* 423, 145–154. <https://doi.org/10.1016/j.epsl.2015.05.014>.

Shinevar, W.J., Behn, M.D., Hirth, G., Jagoutz, O., 2018. Inferring crustal viscosity from seismic velocity: application to the lower crust of Southern California. *Earth Planet. Sci. Lett.* 494, 83–91. <https://doi.org/10.1016/j.epsl.2018.05.014>.

- Wallace, L.M., Beavan, J., McCaffrey, R., Berryman, K., Denys, P., 2007. Balancing the plate motion budget in the South Island, New Zealand using GPS, geological and seismological data. *Geophys. J. Int.* 168, 332–352.
- Wannamaker, P.E., Caldwell, T.G., Jiracek, G.R., Maris, V., Hill, G.J., Ogawa, Y., Bibby, H.M., Bennie, S.L., Heise, W., 2009. Fluid and deformation regime of an advancing subduction system at Marlborough, New Zealand. *Nature* 460, 733.
- Wesnousky, S.G., Scholz, C.H., Shimazaki, K., Matsuda, T., 1983. Earthquake frequency-distribution and the mechanics of faulting. *J. Geophys. Res.* 88, 9331–9340.
- Wessel, P., Smith, W., Scharroo, R., Luis, J., Wobbe, F., 2013. Generic mapping tools: improved version released. *Eos Trans. AGU* 94, 409–410.
- Williams, C.F., DeAngelo, J., 2011. Evaluation of approaches and associated uncertainties in the estimation of temperatures in the upper crust of the Western United States. *Trans., Geotherm. Resour. Council.* 35, 1599–1605.
- Wilson, J.T., 1965. A new class of faults and their bearing on continental drift. *Nature* 207, 343.
- Yang, H., Chemia, Z., Artemieva, I.M., Thybo, H., 2018. Control on off-rift magmatism: a case study of the Baikal Rift Zone. *Earth Planet. Sci. Lett.* 482, 501–509.
- Yin, A., Taylor, M.H., 2011. Mechanics of V-shaped conjugate strike-slip faults and the corresponding continuum mode of continental deformation. *Geol. Soc. Am. Bull.* 123, 1798–1821.
- Yin, A., Xie, Z., Meng, L., 2018. A viscoplastic shear-zone model for deep (15–50 km) slow-slip events at plate convergent margins. *Earth Planet. Sci. Lett.* 491, 81–94.
- Yin, A., Zuza, A.V., Pappalardo, R.T., 2016. Mechanics of evenly spaced strike-slip faults and its implications for the formation of tiger-stripe fractures on Saturn's moon Enceladus. *Icarus* 266, 204–216.
- Zhou, B.B., Liang, X.F., Lin, G.Q., Tian, X.B., Zhu, G.H., Mechie, J., Teng, J.W., 2019. Upper crustal weak zone in Central Tibet: an implication from three-dimensional seismic velocity and attenuation tomography results. *J. Geophys. Res., Solid Earth* 124 (5), 4273–5282.
- Zhu, L.P., Kanamori, H., 2000. Moho depth variation in southern California from teleseismic receiver functions. *J. Geophys. Res., Solid Earth* 105, 2969–2980.
- Zhu, G.H., Liang, X.F., Tian, X.B., Yang, H.F., Wu, C.L., Duan, Y.H., Li, W., Zhou, B.B., 2017. Analysis of the seismicity in central Tibet based on the SANDWICH network and its tectonic implications. *Tectonophysics* 702, 1–7.
- Zuza, A.V., Carlson, C.W., 2018. What can strike-slip fault spacing tell us about the plate boundary of western North America? *Terra Nova* 30, 105–113.
- Zuza, A.V., Yin, A., Lin, J., Sun, M., 2017. Spacing and strength of active continental strike-slip faults. *Earth Planet. Sci. Lett.* 457, 49–62.